SCIENCE CHINA
Chemistry

•REVIEWS•
SPECIAL TOPIC: 2D Materials

October 2018 Vol.61 No.10: 1227–1242
https://doi.org/10.1007/s11426-018-9326-y

Crystal phase control in two-dimensional materials

Jialiang Wang[1], Yang Wei[1], Hai Li[1*], Xiao Huang[1*] & Hua Zhang[2*]

[1]*Institute of Advanced Materials (IAM), Nanjing Tech University (NanjingTech), Nanjing 211816, China;*
[2]*Center for Programmable Materials, School of Materials Science and Engineering, Nanyang Technological University, Singapore 639798, Singapore*

Received May 30, 2018; accepted July 9, 2018; published online September 5, 2018

It is the nature of crystals to exist in different polymorphs. The recent emergence of two-dimensional (2D) materials has evoked the discovery of a number of new crystal phases that are different from their bulk structures at ambient conditions, and revealed novel structure-dependent properties, which deserve in-depth understanding and further exploration. In this contribution, we review the recent development of crystal phase control in 2D materials, including group V and VI. transition metal dichalcogenides (TMDs), group IVA metal chalcogenides and noble metals. For each group of materials, we begin with introducing the various existing crystal phases and their structure-related properties, followed by a detailed discussion on factors that influence these crystal structures and thus the possible strategies for phase control. Finally, after summarizing the whole paper, we present the challenges and opportunities in this research direction.

crystal phase control, metal chalcogenides, noble metals, two-dimensional materials

Citation: Wang J, Wei Y, Li H, Huang X, Zhang H. Crystal phase control in two-dimensional materials. *Sci China Chem*, 2018, 61: 1227–1242, https://doi.org/10.1007/s11426-018-9326-y

1 Introduction

Two-dimensional (2D) materials, such as graphene [1–3] and transition metal dichalcogenides (TMDs) [4–8], have attracted great attention due to their novel properties and functions arising at the reduced dimensions, which may potentially lead to the advancement of future electronics, optoelectronics and energy-related systems [9–11]. Meanwhile, other inorganic 2D materials such as group IVA metal chalcogenides (IVAMCs) and noble metals have also received considerable attention due to their attractive electronic, optoelectronic, catalytic and electrocatalytic properties [12–20].

A common feature of these materials lies in their tunable functional properties that closely correlate to not only their size, shape and composition, but also in particular, their crystal phases [21,22]. A solid material existing in more than one crystalline structure, also termed as polymorphism, has been observed in TMDs (e.g., TiS_2, MoS_2, WTe_2, $TaSe_2$ and NbS_2), IVAMCs (e.g., SnS and SnS_2), III–V semiconducting compounds (e.g., GaAs and InAs) and noble metals (e.g., Ru, Au, Ag and Rh) [23]. For example, group VI TMDs (VITMDs) nanosheets, such as MoS_2 and WS_2, exist in either the hexagonal phase (2H) or the trigonal phase (1T), which exhibit the semiconducting or metallic properties, respectively [4,5]. Some other TMDs, typically group IV (IVTMDs, e.g., TiS_2) and group V TMDs (VTMDs, e.g., TaS_2, $TaSe_2$, $NbSe_2$) have been also found to exhibit in 2H or 1T phase, exhibiting novel superconductivity (SC) or charge density wave (CDW) phases at low temperatures [24,25]. Similarly, a number of phases including hexagonal, trigonal, orthorhombic and cubic structures have been identified in layered IVAMCs (e.g., SnS_2 and SnS), which show phase-

*Corresponding authors (email: iamhli@njtech.edu.cn; iamxhuang@njtech.edu.cn; hzhang@ntu.edu.sg)

dependent electronic band structure and dopant type [14,22,26,27]. As for 2D noble metal nanostructures (e.g., Au and Rh), cubic, hexagonal and tetragonal crystal phases have been revealed, amongst which, those thermodynamically less favored phases show unusual optical properties and outstanding catalytic properties [17,19,28,29]. Moreover, an artificial polymorph of graphene was achieved via a recently developed transfer technique, which exhibited unusual superconductivity [30].

Because of the ultrathin nature of 2D materials, their structures are extremely sensitive to surface defects [31,32], chemical absorption [33,34] and electric charges [35,36]. Therefore, in addition to conventional strategies for phase transition such as thermal annealing [37,38] and applying high pressure [39,40], other approaches such as ionic or atomic doping [41–44], charging [27,45], and ligand exchange [29,46] have been recently demonstrated to achieve effective crystal phase control in 2D materials.

In this contribution, we provide an overview of representative strategies for the crystal phase control of the aforementioned 2D nanomaterials, including TMDs, IVAMCs and 2D noble metals.

2 Transition metal dichalcogenides (TMDs)

Over the past years, single- to few-layer TMDs have demonstrated a number of interesting and important features, such as tunable band gaps [9,37,47], strong spin-orbit coupling [48–50], high catalytic/electrocatalytic activities [51–53], and good mechanical strength [54–56], which make them appealing for both fundamental studies and practical applications [4–8].

TMDs have a general chemical formula of MX_2, where M is a transition metal (such as Ti, V, Nb, Mo, Hf, Ta and W) and X stands for S, Se or Te. Each layer exhibits a "sandwich" type of structure (X–M–X) in which the transition metal (M) is covalently bonded with two chalcogens (X) [5]. Adjacent layers are further bound by weak van der Waals forces which can be feasibly overcome to enable the exfoliation and isolation of single- to few-layered nanosheets [57]. TMDs exist in several structural polytypes (Figure 1), typically involving the trigonal prismatic (1H) or octahedral (1T) coordination [5,58]. With the varied stacking sequence of 1H layers, the hexagonal 2H (i.e., $2H_a$ and $2H_b$) and rhombohedral 3R phases can be achieved, which include two and three X–M–X primary 1H layers, respectively (Figure 1 (b–d)). Besides, two kinds of distorted 1T phase, namely the 1T' and T_d phase, have also been observed, exhibiting the monoclinic (space group $P2_1/m$) (Figure 1(f)) and orthorhombic (space group $Pnm2_1$) (Figure 1(g)) structures. The thermodynamically stable structure for most VITMDs is usually in the $2H_b$ phase, whereas VTMDs are inclined to the $2H_a$ phase [58]. An exception is WTe_2, whose stable bulk phase at room temperature is the orthorhombic T_d phase [59,60].

TMDs exhibit different kinds of electronic characters, including metallic, semimetallic, semiconducting and superconducting behavior, which are highly dependent on their crystal phases. For most VITMDs, while the 2H-phased structures are semiconducting, the 1T (1T', T_d)-phased ones are metal-like [4,5,35,60–62]. Importantly, the semiconducting-phased nanosheets such as MoS_2 have shown large on/off ratios and high carrier mobilities for field effect transistors (FETs) [63,64], whereas the metallic counterparts have been recently found to be highly active towards the hydrogen evolution reaction (HER) [51–53,65]. Moreover, low resistance contacts have been realized by creating 1T (1T')-2H (metal-semiconductor) phase-heterostructures [66,67]. In addition, the phase-dependent CDW phases at low temperatures have been demonstrated in VTMDs, including TaS_2, $TaSe_2$, and $NbSe_2$ [24]. Very recently, an unprecedented polymorph of TaS_2 with an increased CDW transition temperature was revealed by exfoliating a bulk $2H_a$ TaS_2 crystal into ultrathin flakes [68]. Therefore, reliable strategies that can realize phase transition on a large scale are of particular scientific and practical interest.

To date, many methods have been developed to realize

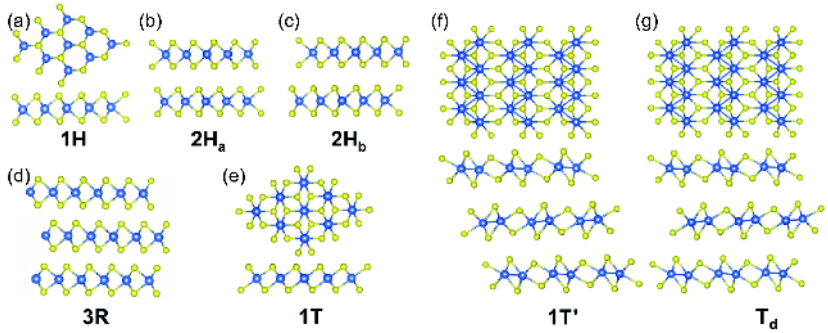

Figure 1 Structural models of transition metal dichalcogenides (TMDs) in their (a) 1H, (b) $2H_a$, (c) $2H_b$, (d) 3R, (e) 1T, (f) 1T' and (g) T_d phases, where blue spheres represent metals and yellow spheres represent chalcogens. In (a, e, f, g), the top part shows the planar view of a single layer, and the bottom part shows the side view of single or few stacked layers. (b–d) Side view of stacked layers (color online).

crystal-phase controlled preparation of TMDs. In this section, strategies including ion intercalation [41,42,53,69–72], charging [45], alloying/doping [43,44,73], defect engineering [32,66,74,75], strain engineering [40,61,76,77], electrostatic gating [35,36], and thermal activation [37,38,78] will be discussed.

2.1 Ion intercalation

TMDs together with other layered materials were found to be chemically intercalatable with a number of alkali metal reagents, such as *n*-butyllithium and metal naphthalenide (metal=Li, Na and K) [79–82]. Intercalation of cations can expand the gap between adjacent TMD layers and thus weaken the van der Waals interaction to enable their isolation via subsequent agitation. The Li-intercalated compounds can also be obtained with our previously developed electrochemical lithiation method, which can be implemented at milder conditions compared to the chemical intercalation method [41,69]. As shown in Figure 2(a), TMD bulk crystals are typically coated on a metal foil (e.g., Cu) and assembled in a Li ion battery cell as the cathode, and a piece of Li foil used as the anode. After discharging, the obtained Li_xMX_2 compounds are immersed and sonicated in water/ethanol to obtain the exfoliated TMD nanosheets.

For both chemical and electrochemical lithium intercalation, the original 2H TMDs have been found to partially transform to the 1T and distorted 1T' phase [52,67,83]. Structural changes in these intercalated compounds in fact have been observed since as early as 1980s [84–87]. With the advancing of electron microscopy techniques, microstructures of these crystal phases can be studied more directly. For example, Eda and co-workers [83] prepared crystal phase heterostructures of MoS_2 via Li-intercalation. Under the Cs-corrected scanning transmission electron microscopy (STEM) imaging, three phases were identified, including the 2H, 1T and 1T' phase consisting of zig-zag chains (Figure 2(b–d)). The mechanism behind the 2H-to-1T (1T') phase transition was then investigated theoretically by several groups [88–91]. In the case of MoS_2 and WS_2, electrons transferred from the alkali metals (e.g. Li, Na, K, etc.) during intercalation could cause an increase in the electron density of the d-orbital of the transition metal, inducing the destabilization of the pristine 2H phase and its transition to the metallic 1T or distorted 1T' phase [92–94].

As an alternative to the post-growth intercalation-induced phase transition, Yu *et al.* [72] recently reported the direct preparation of micrometer-sized 1T'-MoX_2 (X = S, Se) (Figure 2(e–f)) via the sulfurization of potassium molybdate ($KMoO_4$). The high purity 1T'-phase was confirmed by STEM, X-ray diffraction (XRD), and X-ray photoelectron spectroscopy (XPS) analyses (Figure 2(g–h)). The formation and stabilization of the 1T' phase can be attributed to the presence of potassium counterions that may increase the electron density of Mo.

Since electron doping is the main cause to the formation of the 1T (1T') phase, doping agents other than alkali metals such as ammonium containing precursors [42,70] and hy-

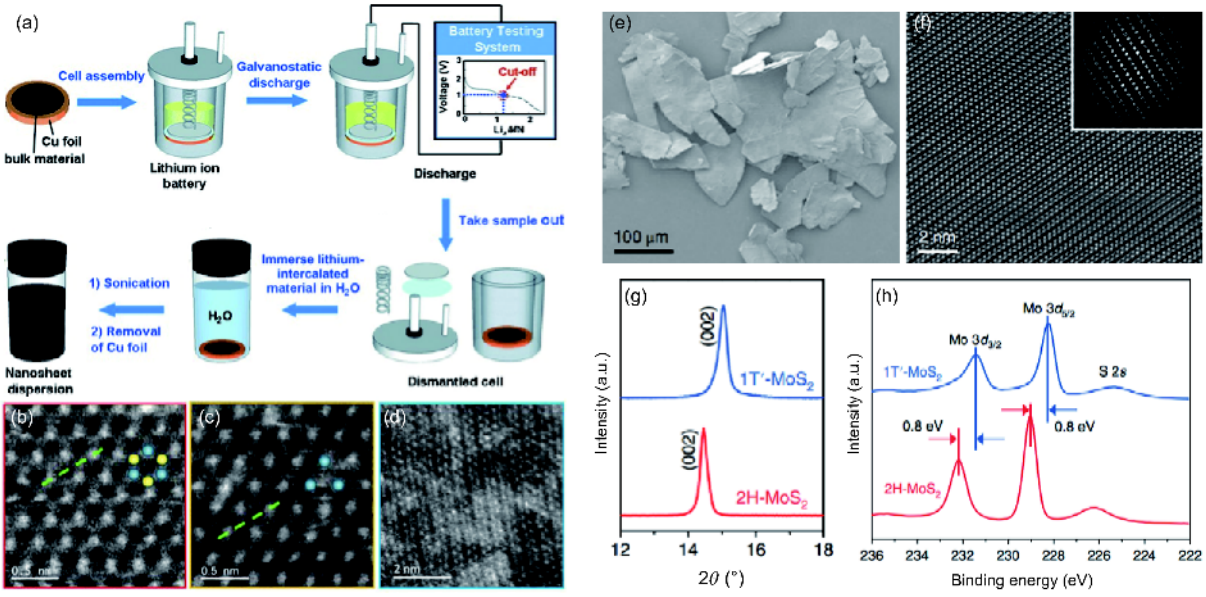

Figure 2 (a) Scheme of the electrochemical lithium intercalation process to produce 2D nanosheets from the layered bulk material [41]. (b–d) High resolution STEM images of (b) 2H, (c) 1T, and (d) 1T' phases. The blue and yellow balls in image (b) and (c) indicate the position of Mo and S atoms [83]. (e) Scanning electron microscopy (SEM) image of the prepared 1T'-MoS_2 crystals. (f) STEM image of a single-layer 1T'-MoS_2 nanosheet. The asymmetric distribution of atoms is clearly shown. Inset: corresponding FFT diffraction. (g) Magnified XRD patterns of the (002) peaks of 1T'- and 2H- MoS_2 crystals. (h) XPS Mo 3d spectra of 1T'-MoS_2 crystals and 2H-MoS_2 crystals obtained by annealing 1T'-MoS_2 crystals [72] (color online).

drazine hydrate [71] have also been used for the *in-situ* preparation of 1T (1T') TMDs. For example, Liu *et al*. [42] reported the synthesis of 1T (1T') phased WS_2 ultrathin nanoribbons (N-WS_2) via a direct hydrothermal reaction between $(NH_4)_{10}W_{12}O_{41}\cdot xH_2O$ and thiourea. In combine with theoretical calculations, they suggested that about 0.75 electrons per NH_4 were transferred to WS_2, resulting in the formation of $WS_2^-\cdot NH_4^+$ ionic complex. With a similar approach, we recently directly synthesized alloyed $Mo_{1-x}W_xS_2$ nanosheets with tunable 1T (1T')/2H phase ratios [70].

2.2 Alloying/doping

Considering the composition-dependence of crystal phases, alloying between TMDs with dissimilar crystal structures is expected to realize phase transitions [44,73]. Due to the fact that WTe_2 is a special case in VITMDs that its thermodynamic stable structure is the T_d phase [60], WTe_2 has been chosen to study the alloying induced phase transitions. For instance, Rhodes *et al*. [44] prepared $Mo_{1-x}W_xTe_2$ alloys with chemical vapor transport (CVT) method and created a simplified phase diagram for the alloying system. It can be seen that the semimetallic orthorhombic phase (T_d) is preferred over the 2H phase for W concentrations (x_c) larger than 0.08 (Figure 3(a–e)). Similarly, Yu *et al*. [73] reported the CVT growth of $WSe_{2(1-x)}Te_{2x}$ (x=0−1) and observed a gradual transition from the 2H to T_d structure with increasing x value, specifically, x=0–0.4 for 2H structure, x=0.5 and 0.6 for mixed 2H and T_d structures, and x=0.7–1.0 for T_d structure (Figure 3(f)).

As for VTMDs, Luo *et al*. [95] reported the synthesis of $TaSe_{2-x}Te_x$ ($0\le x\le 2$) crystals with 2H, 3R, 1T, and monoclinic phases (Figure 3(g)). They found that only a small concentration of Te doping (x=0.02) could lead to 2H-to-3R transition. Interestingly, at $0.1\le x\le 0.35$, the 3R-$TaSe_{2-x}Te_x$ showed the coexistence of superconductivity and a CDW phase at above 0.4 K. At higher Te substitutions ($1.8\le x\le 2$), $TaSe_{2-x}Te_x$ becomes the metallic monoclinic polymorph.

Apart from alloying, doping with elements from different groups with larger atomic disparity could also cause the phase transitions in TMDs [43,88]. Some previous reports showed that MoS_2 would take the 3R phase when minority Mo atoms were substituted by elements like Re or Nb [96]. Besides the 2H-to-3R phase transition, a recent study showed that substitutional Re doping in 2H-phased WS_2 nanotubes could induce their partial transformation to the 1T phase [88]. More recently, Kochat *et al*. [43] reported the chemical vapor deposition (CVD) growth of Re-doped $MoSe_2$ and found that increasing Re concentration stabilized the 1T' phase. This was further supported by density functional theory (DFT) calculations that substitution of each Mo with a Re could lead to the addition of an extra electron which destabilized the 2H phase to transform to the 1T' phase.

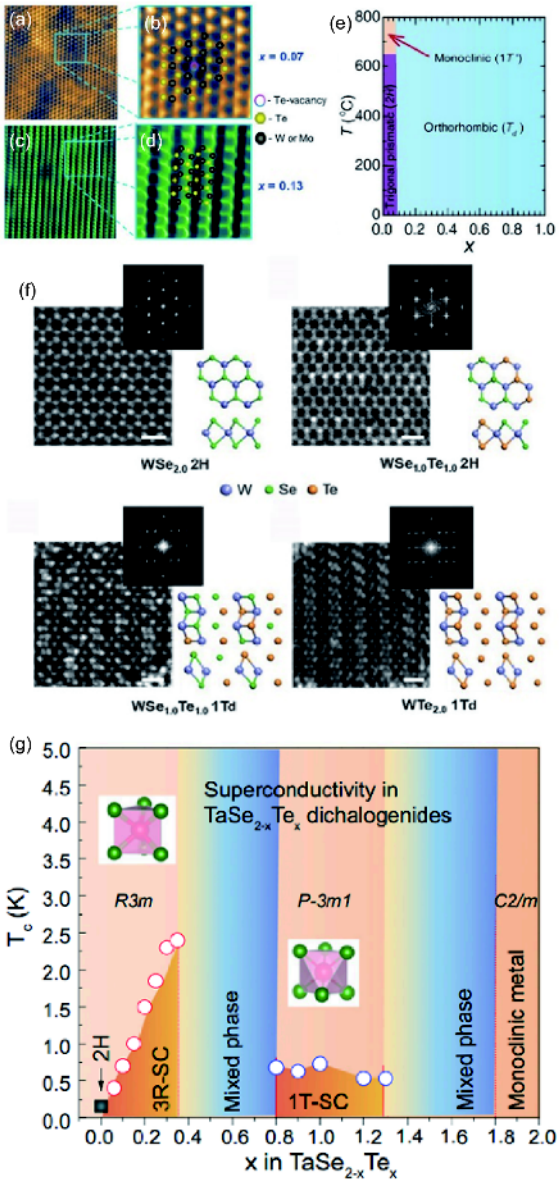

Figure 3 (a) Scanning tunneling microscopy (STM) image of a $Mo_{1-x}W_xTe_2$ single crystal with x=0.07, showing a clear hexagonal pattern as expected for the 2H-phase. (b) Magnification of a local area where one can detect a Te vacancy. (c) STM image of a $Mo_{1-x}W_xTe_2$ single crystal with x=0.13, showing a pattern of parallel chains as expected for the orthorhombic phase. (d) Magnification of a local region revealing the intrachain structure and illustrating the crystallographic positions of transition metal (black dots) and Te (yellow dots) atoms, respectively. (e) Bulk phase-diagram of the $Mo_{1-x}W_xTe_2$ series based on the array of experimental techniques [44]. (f) Atomic resolution STEM characterization of $WSe_{2(1-x)}$-Te_{2x} (x=0–1) alloyed monolayers with different Te concentration [73]. (g) The composition stability ranges of the 2H, 3R, 1T, and monoclinic MX_2 forms in $TaSe_{2-x}Te_x$ and the dependence of T_c on x. The TaX_2 coordination polyhedra are highlighted. Single-phase regions are shown in pink, and multiple-phase regions are shown in blue [95] (color online).

2.3 Defect engineering

Defects in TMDs, typically metal and chalcogen vacancies, can induce profound modification of their chemical, structural and electronic properties [31,32,66,74]. As a typical

example of defect engineering-assisted phase control, Zhou *et al*. [75] found that Te vacancies were created during the growth of $MoTe_2$ when insufficient Te source was provided to react with MoO_3 [66]. This led to the formation of 1T' $MoTe_2$ instead of 2H $MoTe_2$ (Figure 4(a)).

Alternatively, post-growth defect engineering can be implemented to control the phase of TMDs. Up to date, several high-energy sources including electron-beam [74], laser [66] and Ar plasma [32] have been used to generate local structural distortions or atomic defects in TMDs. For example, Cho *et al*. [66] realized a heterophase homojunction between semiconducting 2H and metallic 1T' phase by using laser irradiation to form an ohmic contact in the $MoTe_2$ transistor (Figure 4(b–f)). Theoretical calculations revealed that the phase transition might originate from the Te vacancies at an elevated temperature, and the 1T' phase became more stable than the 2H phase when the Te monovacancy concentration was above 3% (Figure 4(g)).

2.4 Strain engineering

Crystal lattices under strain can be contracted or dilated, leading to the change of relative atomic positions and thus the modification of crystal phases. Duerloo *et al*. [61] theoretically demonstrated the possibility of using mechanical deformation to thermodynamically induce phase transition of VITMDs. It was shown that for most VITMDs, equibiaxial tensile strains of 10%–15% were required to achieve the transition from the semiconducting to the metallic phase [61,97]. As an exception, $MoTe_2$ can be transformed under a minimal tensile strain of only 0.3%–3% at room temperature. This is likely due to the fact that the energy difference between 2H- and 1T'-$MoTe_2$ was approximately only 40 meV based on first-principles calculations, which was much smaller than that of other TMDs [61].

Experimentally, strain has been created in TMDs based on the lattice mismatch between epitaxial films and substrates, by bending of films on flexible substrates, and by applying pressure with an atomic force microscope (AFM) tip or a diamond anvil cell (DAC) [40,61,76,77]. For instance, Nayak *et al*. [40] investigated the effect of pressure on the electronic, vibrational, optical and structural properties of multilayered MoS_2, and found that the multilayered 2H MoS_2 transformed to an intermediate state (IS) at ~10 GPa and then to the metallic phase at > 19 GPa (Figure 5(a, b)). First-principle calculations suggested that the high pressure could cause a reduction in the interlayer spacing and an enhanced S–S interaction, which led to the overlap of the valance and conduction bands (Figure 5(c, d)).

2.5 Electrostatic gating

Li *et al*. [35] pointed out based on DFT calculations, that the reversible 2H-to-1T' phase transition in monolayer TMDs, including $MoTe_2$, MoS_2 and $TaSe_2$, could be induced by electrostatic gating through change of carrier density and electron chemical potential. This was later realized experimentally by Wang *et al*. [36], who demonstrated the 2H-to-1T' phase transition in monolayer $MoTe_2$ placed as the channel in an ionic liquid-gated field effect transistor (FET) (Figure 6(a–d)). Reversible phase transition was demonstrated by increasing or decreasing the gate voltage (Figure 6(c)). Markedly, such phase transition occurred simultaneously across the whole $MoTe_2$ monolayer and the crystal orientation was perfectly preserved (Figure 6(d)).

2.6 Stability of metastable phases

In the above sections, a number of growth and post-growth methods have been employed to obtain metastable phases of TMDs. When sufficient energy is provided, these metastable structures would be converted back to their thermodynamic stable structures, such as through thermal annealing [37,62] and infrared (IR) laser-induced heating [38,78]. For example,

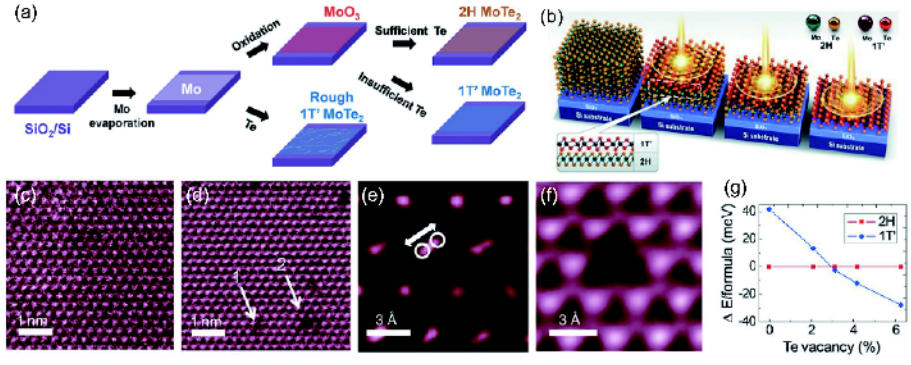

Figure 4 (a) A schematic illustration of the growth process for 1T' and 2H $MoTe_2$ using Mo and MoO_3 as precursors [75]. (b) Schematic representation of the laser-irradiation process. (c) Atomic image of a monolayer of 2H-$MoTe_2$. Bright spheres are Te atoms with hexagonal symmetry. (d) Atomic Te vacancies created artificially. Te single vacancy and divacancy are visible and marked by 1 and 2, respectively. (e) Filtered high-resolution image near a Te vacancy showing the splitting of the Te atoms. (f) Atomic resolution image of a Te divacancy defect. (g) The energy differences between the 2H and 1T' phases as a function of the Te vacancy concentration from the DFT calculation [66] (color online).

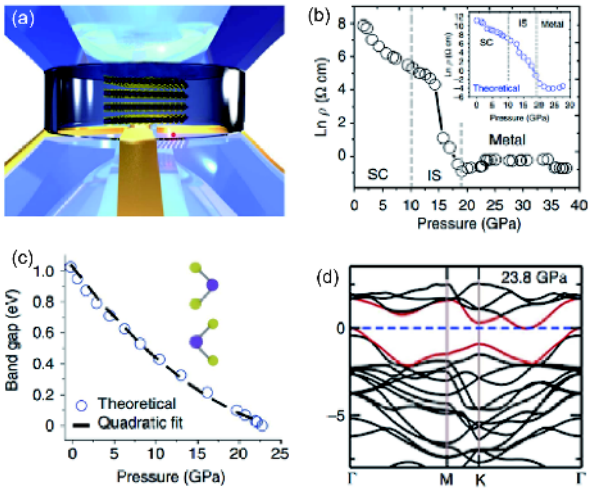

Figure 5 (a) A 3D illustration of multilayered MoS_2 in a DAC pressure medium for compression experiments. (b) Pressure-dependent electrical resistivity of MoS_2. Three characteristic regions have been identified: semiconducting (SC), intermediate state (IS) and metallic regions. Inset: theoretically calculated pressure-dependent electrical resistivity. (c) Theoretical calculation of the pressure-dependent band gap of multilayered MoS_2. (d) Theoretical band structure of multilayered MoS_2 under hydrostatic pressure of 23.8 GPa. VBM and CBM are shown by red lines [40] (color online).

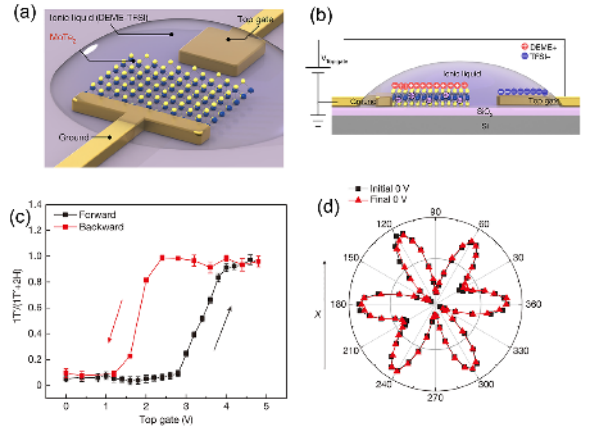

Figure 6 (a, b) Schematics and measurement configuration of a $MoTe_2$ monolayer field-effect transistor. (c) Gate-dependent Raman intensity ratios. The ratio $F = 1T'(A_g)/[2H(A_1')+1T'(A_g)]$ (y-axis) shows hysteresis under an electrical field scan, with a loop width as large as 1.8 V. The black and red curves show increasing and decreasing gate voltage, respectively. (d) SHG intensity from the same monolayer sample as a function of crystal angle. The initial 2H phase at 0 V shows a typical six-fold pattern (black squares connected by a black line) [36] (color online).

the thermally driven transformation of 1T/1T' MoS_2 back to the 2H phase was studied using *in situ* Raman spectroscopy by Guo *et al*. [78]. An activation energy of 400±60 meV (38 ±6 kJ/mol) was calculated for the phase transition based on the temperature dependence of the transformation rate fitted to an Arrhenius expression. Importantly, this analysis revealed that the 1T/1T' phased MoS_2 has a half-life of about 10 d at room temperature and about only 5 h at 400 K.

Surface functionalization of TMDs in metastable phases has recently been demonstrated to improve their stability [33,34]. For example, Voiry *et al*. [33] used organic halides or I_2 to covalently or non-covalently functionalize the electron-rich metallic 1T TMDs, respectively, both leading to the quenching of their negative charges and thus the improved stability (Figure 7(a)). In addition, it is worth noting that after functionalization, while the lattice structure of the 1T phase remained unchanged, its electronic property is remarkably altered from metallic to semiconducting, giving rise to a strong and tunable photoluminescence (Figure 7(b, c)).

Unfortunately, the improved stability is usually at the expense of surface chemical/electrochemical activities. Very recently, Benson *et al*. [34] systematically investigated the correlation between the electron donating strength of the surface ligands and the surface energetics, electron transfer resistance, and the HER catalytic activity of thus-functionalized 1T-MoS_2 nanosheets (Figure 7(d, e)). They found that although 1T-MoS_2 could be substantially stabilized by covalent surface functionalization, its HER catalytic activity was greatly suppressed due to appreciable reduction in its electron density. More evidently, the loss of HER activity became severer when the 1T-MoS_2 was functionalized by ligands with higher electron withdrawing ability.

3 Layered group-IVA metal chalcogenides

As an important sub-group of 2D layered materials, group-IVA metal chalcogenides (IVAMCs, metal=Ge, Sn; chalcogen=S, Se, Te) have aroused intensive research interest due to their attractive electronic and optoelectronic properties, combined with earth abundancy, low cost, and environmental friendliness [12–16].

According to the metal/chalcogen stoichiometric ratio, IVAMCs take either the formula of MX (e.g., GeS, GeSe, SnS, SnSe, SnTe,) or MX_2 (e.g., GeS_2, $GeSe_2$, SnS_2, $SnSe_2$) [22]. Hexagonal, trigonal, orthorhombic and monoclinic crystal structures have been identified in IVAMCs [27,98–102]. Taking SnS as an example, it exists in two polymorphous crystal phases, namely orthorhombic (space group *Pnma*) and cubic phase (space group *Cmcm*) (Figure 8) [101]. Differently, SnS_2 can crystallize into the trigonal or hexagonal structure in which one monolayer of Sn atoms are sandwiched by two layers of S atoms, and similar to TMDs, depending on the type of Sn–S coordination as well as the stacking sequence of the adjacent S–Sn–S layers, 1T, 2H, and 4H polytypes of SnS_2 have been reported [26,27,98,99].

Although unlike TMDs, IVAMCs are semiconductors regardless of their phases, their semiconducting properties, in terms of bandgaps and dopant type, vary distinctively with crystal phases [12–15,26,27,103–108]. For example, SnS is a p-type semiconductor with narrow direct and indirect band gaps of 1.3 and 1.07 eV, respectively, resulting in a high

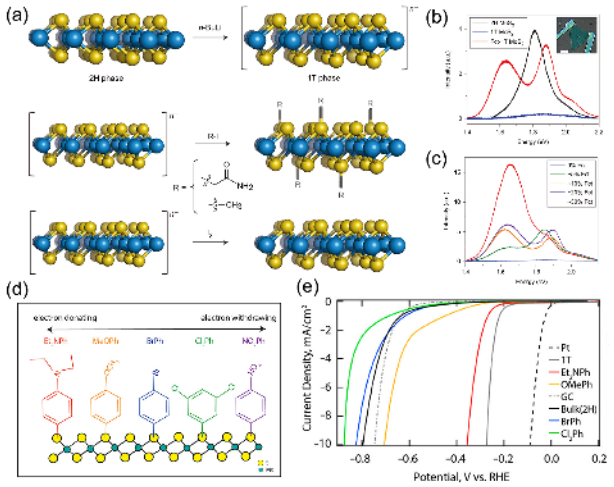

Figure 7 (a) Schematic of functionalization scheme. (Row 1) The 2H phase of TMDs is converted to the 1T phase via lithiation using butyllithium (BuLi), and the 1T phase is negatively charged. n^- indicates the excess charges carried by the exfoliated 1T-phase nanosheets. (Row 2) The nanosheets are functionalized using 2-iodoacetamide or iodomethane (R-I) solution. (Row 3) The charge on the nanosheets can also be quenched by reacting with iodine, with no covalent functionalization. (b) Photoluminescence spectra obtained from single-layer MoS_2 grown by CVD (2H phase), from the metallic 1T phase and from the functionalized 1T phase. (c) Modulation of photoluminescence peak intensity with increasing amount of functionalization: blue, 0% Fct; green, ~5% Fct; orange, ~10% Fct; purple, ~20% Fct; red, ~30% Fct. Photoluminescence peaks are normalized to the Raman peak of silicon at 520 cm^{-1} [33]. (d) Schematic of the various functional groups on 1T MoS_2. (e) Linear sweep voltammograms (LSV) for glassy carbon electrodes deposited with functionalized, 1T, and bulk (2H) MoS_2 [34] (color online).

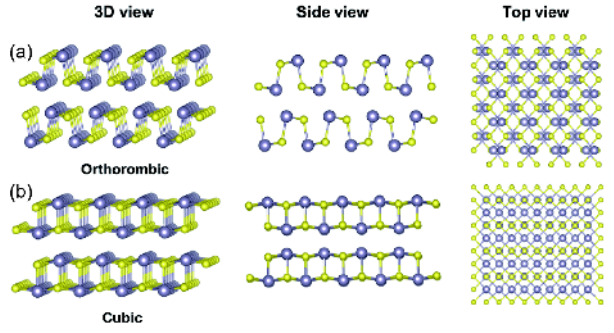

Figure 8 Structural models of layered orthorhombic (a) and cubic (b) phased IVAMCs. The left, middle and right columns show the 3D-view, side view and top planar view, respectively (color online).

absorption coefficient in the near-infrared spectral range for photodetectors, solar cells, photothermal therapy and so on [103,104]. Importantly, its puckered in-plane structure gives rise to highly anisotropic optical and electronic properties [105,106]. In sharp contrast, SnS_2 is an n-type semiconductor and possesses a symmetric in-plane structure and thus isotropic optical properties with an indirect bandgap of ~2.2–2.7 eV [26,27]. SnS_2 nanosheets or nanoplates have exhibited high-mobility with large on-off ratios for field-effect transistors (FETs) [26], fast photo-response for photodetectors [15,108] and large theoretical specific capacity for metal-ion batteries [12,109,110].

Therefore, it is essential to control the crystal phases of IVAMCs for further broadening their applications. Various methods such as mechanical exfoliation [26], vapor-transport deposition (VTD) [100,102,111], and wet chemical synthesis [13,112] have been employed for the preparation of monolayer or few-layer IVAMCs. In the following paragraphs, we will discuss the factors that control the crystal phase of the IVAMCs during or after growth, especially through the change of temperature [14,113–115], using reducing agent [27] and e-beam irradiation [116].

3.1 Thermal effect

Temperature is always a deterministic factor affecting crystallization of materials. Taking SnS_2 as an example, previous reports suggested that low-temperature (e.g., <600 °C) synthesis is beneficial to the formation of the 2H-polytype, while intermediate temperatures favor the 18R phase and high temperatures above 800 °C lead to 4H-SnS_2 [99,117]. As for SnSe, which exhibits the low temperature orthorhombic phase and high temperature cubic phase [14,118–120], Zhao *et al*. [14] demonstrated the reversible phase transition between them by heating the sample from room temperature to ~800 K and then cooling it back to room temperature (Figure 9(a–c)).

In addition, transition between MX and MX_2 can also be realized via temperature control. Fernandes *et al*. [113] found that selenization of magnetron sputtered Sn at 300–470 °C favored the growth of hexagonal-phased $SnSe_2$, and at higher temperatures of ~530–570 °C, orthorhombic SnSe became the major product. Similarly, Huang *et al*. [114] reported the synthesis of diverse shaped and phased $SnSe_x$ by controlling the substrate temperature in a CVD process. As shown in Figure 10(a–j), on the substrate near the high temperature zone, square-shaped orthorhombic SnSe nanosheets were obtained, and those on the substrate with lower temperatures, hexagonal, truncated triangular and triangular nanoplates in the hexagonal phase were synthesized. This phenomenon was attributed to the fact that, at higher temperatures, adsorbed Se atoms were likely desorbed more quickly into the carrier gas, which led to the formation of SnSe instead of $SnSe_2$.

Besides controlling the growth temperature, post-growth thermal annealing can cause phase transitions as well. For example, Zhou *et al*. [115] heat-treated SnS_2 in Ar atmosphere and achieved SnS structures due to the depletion of S by partial sublimation and dissociation of SnS_2. Importantly, by taking the advantage of the thermal induced phase transition, Tian *et al*. [121] recently reported the creation of in-plane p-n heterostructures by selectively thermal conversion of $SnSe_2$ to SnSe in vacuum. The junction between the

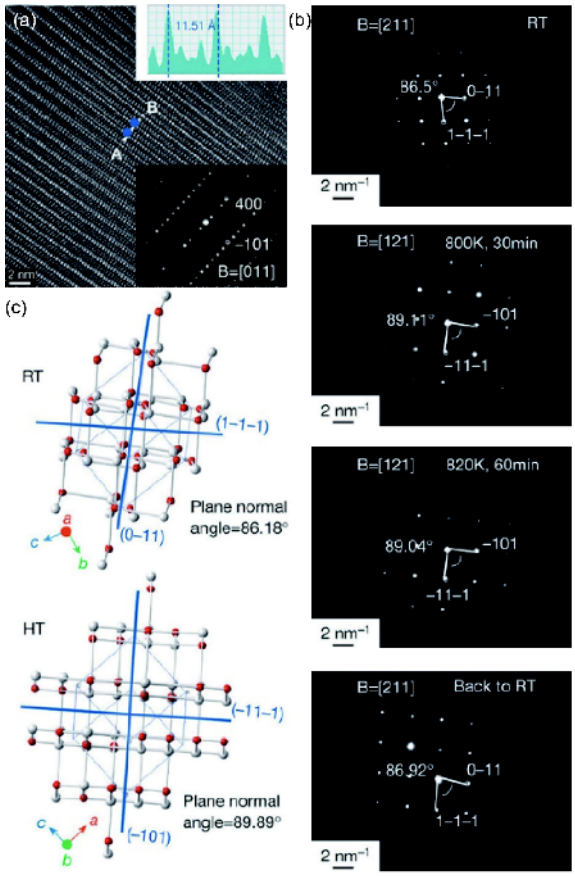

Figure 9 (a) Main panel, high-resolution transmission electron microscopy (HRTEM) image of single-crystal SnSe (scale bar, 2 nm). Bottom inset, corresponding diffraction pattern along the [011] zone axis; top inset, the line profile (distance is plotted in Å, *y* axis) along the dotted line AB in the main panel showing the d spacing of (100). (b) Simulated crystal structures of the phase at room temperature (RT; *Pnma*) and at high temperature (HT; *Cmcm*), viewing along the [211] and [121] directions; planes (1-1-1), (-101) and (0-11) are marked by blue lines. (c) Diffraction patterns obtained at different temperatures. B, zone axis. There is a difference in measured angle between (1-1-1) and (0-11) of about 2.6° between room and elevated temperatures [14] (color online).

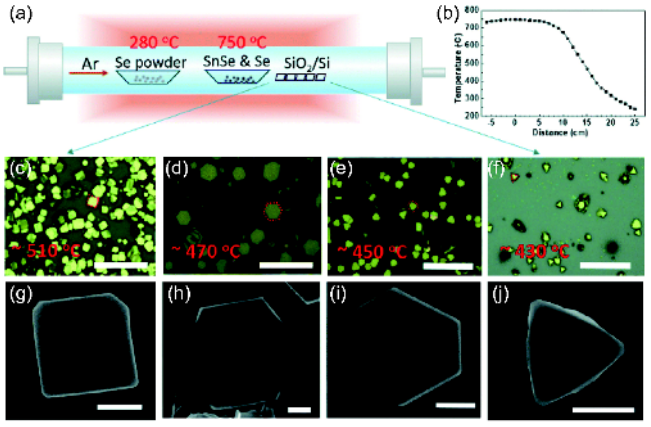

Figure 10 (a, b) The experimental setting and various nanosheets grown on SiO_2/Si substrates. (a) The schematic of the experimental setups. (b) The temperature gradient in the furnace. The middle of the second heating zone is defined as the origin. (c–f) The optical images of the as-grown nanosheets. (g–j) The corresponding SEM images of NSs. Scale bar: (c-f) 30 μm, (g) 0.5 μm, (h, i, j) 2 μm [114] (color online).

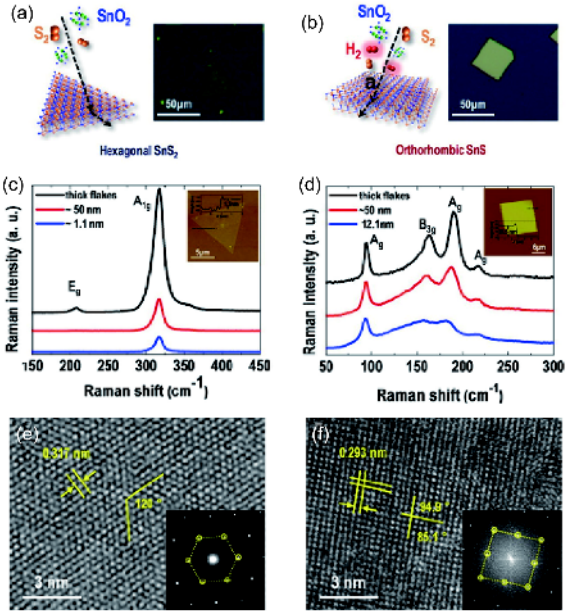

Figure 11 Growth schematics and representative optical microscope images of (a) hexagonal 2D SnS_2 in N_2 and (b) orthorhombic 2D SnS in N_2–H_2. Raman spectra of (c) SnS_2 2D crystals and (d) SnS 2D crystals of various thickness. Insets: atomic force microscope images. HRTEM images of (e) a SnS_2 crystal and (f) a SnS crystal. The corresponding FFT-diffraction patterns of the insets clearly show the hexagonal and orthorhombic lattices [27] (color online).

hexagonal $SnSe_2$ and orthorhombic SnSe formed atomically sharp interface, as confirmed by scanning tunneling spectroscopy (STM) measurement. Notably, $SnSe_2$ was found to be heavily n-doped due to Se vacancies and interstitial Sn, whereas SnSe was p-doped due to Sn vacancies and interstitial Se.

3.2 Reducing environment

Given the fact that the oxidation state of Sn in SnS is +2, smaller than that in SnS_2 (+4), preferred growth of SnS may be achieved in a reducing environment. Recently, Ahn *et al.* [27] reported the controllable CVD growth of hexagonal SnS_2 or orthorhombic SnS by altering the ratio of H_2/N_2 gas, which carried S vapor to react with SnO_2 on substrate (Figure 11(a–f)). It was found that rectangular SnS crystals were obtained when the H_2/N_2 ratio was larger than 0.4. Below that, the products became irregularly shaped. When no H_2 was introduced, hexagonal phased SnS_2 crystals in the triangular shape were obtained.

3.3 E-beam irradiation

It has been suggested that e-beam irradiation during transmission electron microscopy (TEM) analysis can cause a

local temperature rise to ~500 °C. Recently, Sutter *et al.* [116] reported electron-beam induced vacancy formation and transition of trigonal (1T) phased SnS_2 to orthorhombic SnS. Few-layer SnS_2 was found to first transform to a Sn_2S_3 intermediate and then to SnS (Figure 12(a–f)). It is worth noting that the appearance of Sn_2S_3 intermediate caused rotational realignment of atoms and resulted in the tilted (21° off-axis) SnS. For ultrathin SnS_2 (<3 layers), the Sn_2S_3 intermediate was not observed, leading to the formation of *c*-axis oriented SnS. Similar to SnS_2, $SnSe_2$ also underwent e-beam induced phase transition to SnSe, but without the formation of any Sn_2Se_3 intermediate. This observation was supported by phase diagrams previously created by Sharma *et al.* [122], which indicated that while Sn_2S_3 can exist under thermal equilibrium, Sn_2Se_3 can not.

4 Noble metals

The progress made in graphene and 2D layered inorganic semiconductors has provoked research in other 2D systems.

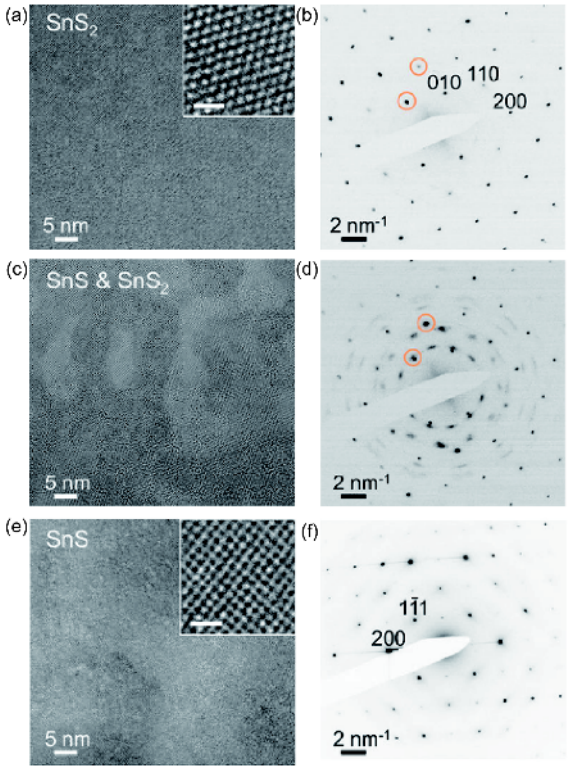

Figure 12 Evolution of few-layer SnS_2 under electron-beam irradiation. (a) HRTEM image of a thin area in a SnS_2 flake. (b) HRTEM image of the same flake after 200 keV electron-beam exposure at room temperature for 12 min. (c) TEM image of the flake after 200 keV electron-beam exposure at 300 °C for 36 min. (d) Electron diffraction pattern showing the SnS_2 crystal structure along [001] zone axis. (e) Diffraction pattern showing a superposition of the original SnS_2 reflections and additional reflections that can be indexed to the orthorhombic α-SnS crystal structure. (f) Diffraction pattern indexed to single crystalline orthorhombic α-SnS crystal structure along the [011] zone axis. Scale bars of panels (a) and (c) insets: 1 nm [116] (color online).

For example, noble metals in the 2D form have exhibited structural and chemical properties distinctive from their bulk counterparts, and found a wide range of applications such as energy conversion, surface enhanced Raman scattering, biosensing, photothermal therapy and catalysis [17,19,20,28,29,123–126].

The thermodynamically stable phases vary for different noble metals [21]. While Au, Ag, Pd, Pt, Rh and Ir normally crystalize in the highly symmetric fcc structure, other metals, typically Ru and Os, prefer the hcp structure (Figure 13(a)). In addition to the commonly observed phases, i.e., fcc and hcp-2H, other phases including hcp-4H and face-centered tetragonal (fct) have also been identified in noble metals [28,29,127]. The fcc, 2H and 4H phases all belong to the close-packed systems, and only differ in the stacking sequence of the close-packed planes (Figure 13(b)).

As known, the functional properties of noble metal nanostructures can be tuned by their size [128], shape [129,130], composition [131,132] and crystal phase [127,133,134]. For instance, a thin film of 4H Ag showed over 100 times larger in-plane resistivity and much stronger visible-light absorption compared with that of the common fcc Ag films [133] hcp Ru nanoparticles (NPs) are more active to catalyze CO oxidation than fcc Ru NPs with the similar size [134]. FePt NPs exhibited a property transition from superparamagnetic to strongly ferromagnetic when they underwent a transformation from fcc to an unusual fct structure [127]. Therefore, controlling the crystal structure of noble metals and understanding the mechanisms behind phase control are of paramount importance.

In the following context, we will discuss the effect of thickness [28,29,135], surface ligands [19,29,46,136], metal coating [46,137,138] as well as pressure [39,139] on the crystal phase of 2D noble metals.

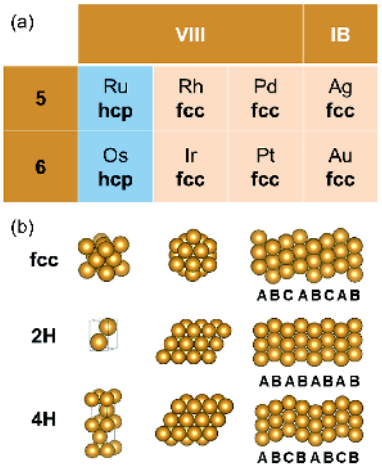

Figure 13 (a) Crystal phase periodic table for noble metals. (b) Structural models for fcc, 2H and 4H phases for noble metals. The left, middle and right columns show the unit cell 3D view, close-packed plane top-view, and side-view showing the packing sequence of close-packed planes, respectively (color online).

4.1 Size effect

Both theoretical and experimental investigations have showed that when one of the dimensions of a crystal is reduced to the nanoscale, its surface energy can dominate the total systemic energy and unusual crystals phases that are absent or metastable in the bulk form may be revealed [128,140,141].

This is elaborated in our previous reports on the synthesis of 2H phased ultrathin Au square sheets (AuSSs) and 4H phased Au nanoribbons (NRBs) [28,29,135]. In the case of 2H AuSSs [28], they were synthesized from heating a mixture solution containing graphene oxide sheets, $HAuCl_4$, oleylamine, hexane and ethanol at 55 °C. The AuSSs exhibited an edge length of 200–500 nm and a thickness of only ~2.4 nm, corresponding to ~16 Au atomic layers (Figure 14 (a, b)). Detailed TEM analyses proved that the AuSSs were pure hcp structures. Importantly, by prolonging the growth time, when the thickness of an AuSS increased from ~2.4 to ~6 nm, fcc domains began to appear. Alternatively, the thickness of the hcp AuSSs could also be increased through a secondary growth of Au on them [135]. The obtained Au square-like plates demonstrated the alternating hcp/fcc structure in their center region with a thickness of ~5 nm and a pure fcc structure in their 7.3 nm-thick edge areas (Figure 14(c–e)), revealing a thickness-dependent structural property.

By introducing 1,2-dichloropropane to the growth solution containing $HAuCl_4$, oleylamine and hexane, our group [46] prepared ultrathin Au nanoribbons (NRBs) with an unprecedentedly observed 4H structure for Au. The time-dependent characterization of intermediate products showed that ultrathin Au nanowires (Au NWs) with a diameter of 1.4–2.0 nm were formed first at the reaction time of 4 h, and showed short-range 2H structural domains along with many stacking faults (Figure 14(f)). As the reaction proceeded to 8 h, these Au NWs grew into ribbon-like nanostructures with a width of 2.8–5.8 nm (Figure 14(g)), and at this stage, hexagonal 4H domains already existed. The final Au NRBs with widths of 8.0–20.0 nm showed the 4H phase over their entire structures after 12 h of reaction (Figure 14(h)). The fact that the 2H structure gradually evolved to the 4H structure with increasing ribbon width suggests that the 4H Au is relatively more stable compared with the 2H Au. This agrees with previous theoretical calculations that 4H Au processes larger cohesive energy per atom than the 2H counterpart [142].

Very recently, we also prepared ultrathin Ru nanoblades with an intergrown fcc/hcp structure by using Cu salt as a co-reduction and sacrificial reagent [143]. The Ru nanoblades with a thickness of ~2 nm showed basal planes normal to the close-packing $[111]_f$ or $[001]_h$ directions, suggesting a faulty stacking of the two phases. Control experiments further indicated that by annealing the ultrathin Ru nanoblades, they transformed into larger nanoparticles showing exclusively the thermodynamically stable hcp structure.

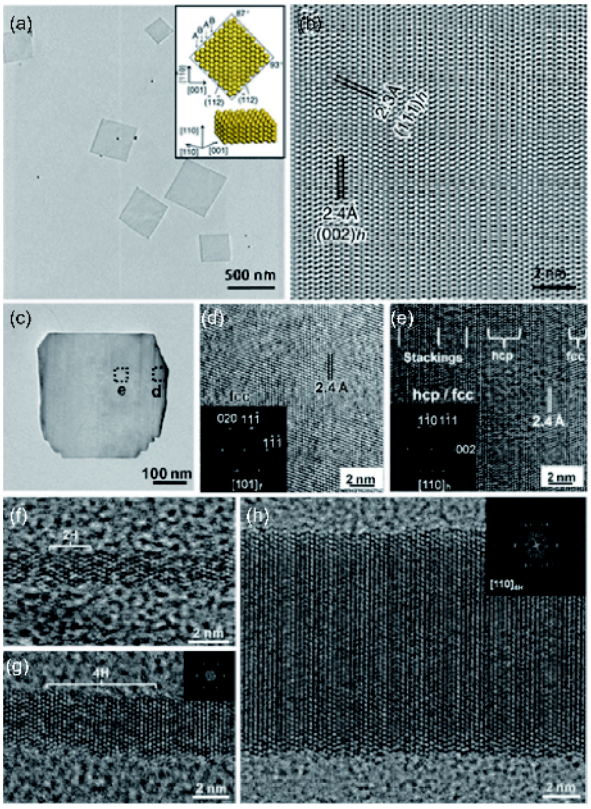

Figure 14 (a) TEM image of ~2.4 nm thick AuSSs on a GO surface. (b) HRTEM image of a small region of a typical AuSS oriented normal to $[110]_h$ [28]. (c) TEM image of a typical AuSP synthesized on GO. (d, e) HRTEM images of the areas designated in (c). Insets in (d, e): Fast Fourier transform (FFT) generated selected area electron diffraction (SAED) patterns of the corresponding HRTEM images in (d, e) [135]. (f) 2H structure and stacking faults were observed at the reaction time of 4 h. (g) 4H structure appeared at the reaction time of 8 h. Inset: the corresponding FFT pattern of the marked 4H domain in (g). (h) The 4H structure were obtained at the reaction time of 12 h. Inset: the corresponding FFT pattern of the HRTEM image shown in (h) [29] (color online).

4.2 Ligand effect

Because the surface energy of an ultrathin nanostructure may dominate its total systemic energy, surface ligands are expected to exert crucial effects on its chemical and structural stability [128,144]. In fact, the effect of size usually comes hand-in-hand with the effect of surface functionalization. Very recently, Li *et al.* [19] solvothermaly synthesized unusual hcp Rh nanosheets which were about 500–600 nm in edge length (Figure 15(a–c)). Extended X-ray absorption fine structure (EXAFS) analysis of the nanosheets indicated that the Rh atoms possessed a small coordination number of ~6.4, suggesting that they were single atomic layers. Theoretical calculations suggested that these single layer nanosheets were likely stabilized by the surface adsorbed

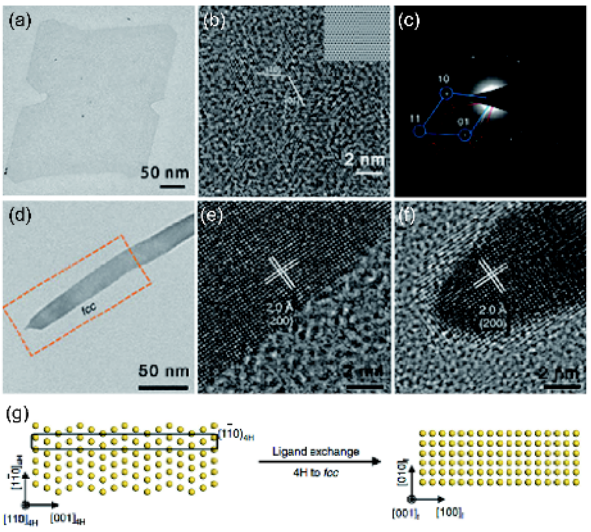

Figure 15 (a) High-magnification TEM images of hcp Rh nanosheets. (b) Aberration-corrected HRTEM image of hcp Rh nanosheets. Inset: the-corresponding filtered HRTEM image using the crystallographic method. (c) A typical SAED pattern of hcp Rh nanosheets [19]. (d) A typical TEM image of an Au NRB after the ligand exchange. (e, f) HRTEM images taken from the edge and end of the marked region in (d), respectively. (g) Schematic illustration of the ligand exchange induced phase transformation of 4H Au NRBs [29] (color online).

polyvinylpyrrolidone (PVP) molecules which considerably decreased the surface energy of Rh from 0.126 to 0.071 eV $Å^{-2}$. Evidently, without presence of PVP, Rh nanosheets were aggregated. In addition, CO molecules, which were produced via decomposition of formaldehyde in the growth solution at elevated temperatures, were suggested to strongly interact and stabilize the Rh nanosheets. The use of CO as stabilizing agent has been demonstrated previously in the synthesis of ultrathin Pd nanosheets by Huang and coworkers [17]. In another report, by reducing $Pt(acac)_2$ and $Bi(NE)_3$ with oleylamine in the presence of NH_4Br, Hou *et al*. [136] obtained colloidal of polycrystalline hcp BiPt nanoplates. The BiPt nanoplates showed a lateral size of ~42 nm and a thickness of ~6 nm. Importantly, the Br^- ions were suggested to adsorb on the (101) planes of PtBi, preventing the nanostructures from growing along the [101] direction, and thus forming the anisotropic nanoplates. Besides, halide ions such as Cl^- or I^- except for F^- were found to exert the similar effect.

Because of the crucial effects of surface ligands, ligand exchange has been explored in order to control the crystal phase of ultrathin Au structures. For example, the aforementioned AuSSs were originally capped with oleylamine molecules from their synthetic solution. We found that if the oleylamine was replaced with thiols (e.g., octadecanethiol, ODT), which bond more strongly with Au surfaces by forming Au–S bonds, the hcp AuSSs were transformed to the pure fcc AuSSs with a [100] orientation showing the typical square lattice pattern [46]. Interestingly, this phase transition caused a thickness increase and lateral size reduction in AuSSs, due to the enlarged lattice spacing from the initial $d_{(110)h}$=1.5 Å to the final $d_{(200)f}$=2.0 Å if the number of atomic layers was kept consistent during the transition. It is worth noting that a sufficiently high concentration of ODT molecules in the solution is needed to ensure a rapid and complete exchange of oleylamine with ODT ($\geqslant$ 20 mM), and thus a uniform phase transformation over the entire structure of the hcp AuSS. Otherwise, poorly crystallized Au nanostructures with irregular shapes were obtained, probably due to non-uniform ligand exchange induced in-plane strain. The thiols that can induce phase transformation of AuSSs are not limited to ODTs, but other thiols regardless of the lengths of n-alkane chains ($3<n<18$), the functional groups (carboxylic acid, hydroxide or benzene), and the number of thiol groups (monothiol or dithiol), can also be used.

Similarly, by applying ligand exchange, transformation of the 4H Au NRBs to the fcc NRBs was also realized [46]. The TEM images of the resulting fcc NRBs and the transformation schemes are shown in Figure 15(d–g). From the scheme we can see that, the transition of 4H-to-fcc transition can be described as the flattening of the $(1–10)_{4H}$ planes. This observation agrees with previous findings that thiols (or sulfur-containing molecules) can bond with surface Au atoms and induce their reconstruction to generate a metal layer with higher coordination number [145,146].

4.3 Metal coating

The surface properties of metal structures could be significantly altered by epitaxially depositing a different metal [147–149]. Note that this strategy has recently been applied to realize various bimetallic nanomaterials with controllable crystal phases, e.g., hcp/fcc or fcc Au@Ag square sheets [46], fcc Au@M (M=Pt, Pd) rhombic nanoplates [137], 4H/fcc Au@M NRBs (M=Ag, Pd, Pt) [46], as well as 4H/fcc Au@ M (M=Ir, Rh, Os, Ru and Cu) [138].

Taking hcp AuSSs as an example, depositing Ag on its surface can result in two different types of phase transformation depending on the kind of reducing agent used for Ag reduction [46]. In the case of using reducing agents such as *L*-ascorbic acid or $NaBH_4$, the pure hcp AuSSs were transformed to the pure $(100)_f$-oriented fcc Au@Ag core-shell square sheets based on TEM, HRTEM, SAED and energy dispersive X-ray spectrometry (EDS) analyses (Figure 16(a–d)). This kind of transition proceeds via the flattening of the $(11\text{-}0)_{2H}$ planes, which assembles that of ligand exchange induced phase transition mentioned above. In contrast, when oleylamine was used to reduce Ag, hcp AuSSs were grown into the $(110)_h/(101)_f$-oriented hcp/fcc mixed Au@Ag nanosheets (Figure 16(f–i)). This type of phase transformation proceeds via the change of packing sequence of closed-packed planes, similar to the martensitic transition, leading

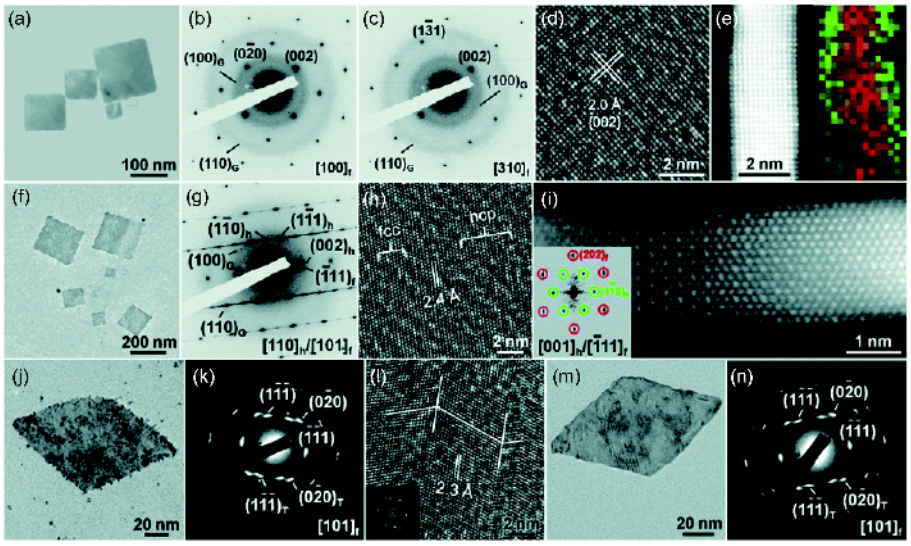

Figure 16 (a) Bright-field TEM image of typical fcc Au@Ag square sheets on GO sheets. SAED patterns taken along the $[100]_f$ (b) and $[310]_f$ (c) zone axes of an fcc Au@Ag square sheet. (d) A typical HRTEM image of fcc Au@Ag square sheet. (e) Aberration-corrected high-angle annular dark-field scanning transmission electron microscopy (HAADF-STEM) image and the corresponding overlapped STEM-EDS elemental mapping (Au: red color; Ag: green color) showing the cross-section of a typical fcc Au@Ag square sheet. (f) Bright-field TEM image of typical hcp/fcc Au@Ag square sheets on GO sheets. (g) SAED pattern and (h) HRTEM image of a representative hcp/fcc Au@Ag square sheet. (i) Aberration-corrected HAADF-STEM image of the cross-section of an hcp/fcc Au@Ag square sheet collected along the $[001]_h/[\bar{1}11]_f$ zone axes. Inset: the corresponding FFT pattern of the HAADF-STEM image shown in (i) [46]. (j) TEM image, (k) SAED pattern and (l) HRTEM image of a typical fcc Au@Pt rhombic nanoplate. Inset in (l): the corresponding FFT pattern of the HRTEM image shown in (l). (m) TEM image and (n) the corresponding SAED pattern of a typical fcc Au@Pd rhombic nanoplate [137] (color online).

to an intergrowth of hcp and fcc domains [28,135]. Importantly, it was also found that the mixed hcp/fcc Au@Ag square sheets could be obtained by using octylamine (a primary amine), whereas the reduction with dioctylamine (a secondary amine) led to the formation of pure fcc $(100)_f$-oriented Au@Ag nanosheets. These experimental results suggested that primary amines may favor the formation of hcp-containing structures [150,151].

Interestingly, unlike coating hcp AuSSs with Ag, which resulted in either the $(100)_f$-oriented or $(110)_h/(101)_f$-oriented hcp/fcc mixed Au@Ag nanosheets, coating AuSSs with Pt and Pd led to the production of fcc Au@Pt and Au@Pd core-shell rhombic nanoplates with high density of twins and stacking faults (Figure 16(j–n)) [137]. This difference might be due to the larger lattice mismatch between Pt or Pd and Au (~5.8%), compared to that between Ag and Au (~0.2%). Note that a small amount of fcc $(100)_f$-oriented Au@Pt or Au@Pd square nanoplates (<10% yield) was also obtained in the final products.

In addition to hcp AuSSs, 4H Au NRBs have also been used to prepare bimetallic structures, namely 4H/fcc Au@M (M=Ag, Pt, Pd as well as Ir, Rh, Os, Ru and Cu) structures [29,138]. However, a complete phase transition from 4H to fcc structures was not observed in these attempts, and mixed 4H/fcc Au@M NRBs were mostly obtained, indicating that 4H Au nanostructures are relatively more stable than that of hcp (2H) phase. This was also reflected from our previous findings that 2H Au nanosheets or nanowires were more easily destroyed under e-beam irradiation compared to 4H nanoribbons [28,152].

4.4 High pressure

High pressure has enabled phase transition in many materials such as TMDs [40,153], GaAs [154] and BiTeI [155,156]. Normally, bulk crystals of noble metals show good tolerance towards moderate pressures, largely due to their highly symmetric and close-packed crystalline structures. For instance, submillimeter fcc crystals of Ag, Au, Pt, Pd, and Cu are stable when subjected to pressure up to 91.8, 182, 304, 77.4, and 188 GPa, respectively, at room temperature [157,158]. However, nanostructured noble metals are more prone to pressure induced structural change [39,139,159]. For example, Sun *et al*. [39] reported the preparation of Ag nanplates based on a galvanic reaction between a heavily doped n-type GaAs wafer and $AgNO_3$ aqueous solution. The nanoplates exhibited multiple hcp twin planes in the dominating fcc structure. Under increasing pressure up to 1.03 GPa, the hcp domains associated with the twin planes disappeared to give a pure fcc structure as evidenced in the XRD pattern (Figure 17(a)). During this process, the Ag nanoplates were broken into smaller domains (typically <50 nm), resulting in the loss of the multiple twin planes (Figure 17(b)). The fractured Ag nanocrystals further transformed to fct structures as the pressure was further increased up to 12 GPa.

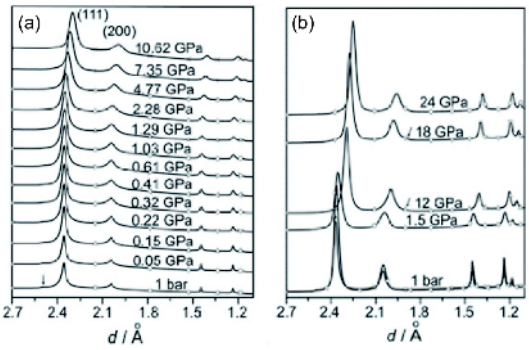

Figure 17 (a) XRD patterns of the as-grown Ag nanoplates on the wafer obtained during compression with small steps. (b) XRD patterns obtained with large steps [39].

5 Conclusions

In summary, we have discussed the recent development of strategies used for the crystal-phase controlled growth or post-growth treatment of 2D TMDs, VIAMDS and noble metals. For TMDs, their phase transition can be realized via ion intercalation, alloying/doping, electron injection, electrostatic gating, defect engineering, strain engineering and so on. In contrast, the crystal-phase control of IVAMCs has been mostly relying on thermal methods. Although solid-state phase diagrams can guide the variation of temperature, other factors such as growth substrate, use of reducing agent, amount of and ratio between reactants could also affect the final products. Defects, such as chalcogen vacancies, could be created via thermal treatment as well as e-beam irradiation, leading to the stoichiometric transition from MX_2 to MX. As for 2D noble metals, in addition to conventional strategies involving high energies, such as high pressure and high temperature treatments, exchange of surface ligands and secondary growth of similar metals can be easily implemented to induce phase transitions at mild conditions.

In spite of the progress made in this research direction, challenges remain to be resolved. Stability is one of the most important issues, as the metastable crystal structures might revert back to the thermodynamically stable ones under the influence of high temperature or other external perturbations. Although surface functionalization can modify their surface energy and improve stability, it severely sacrifices their functional performances, especially in applications that require surface activity. As another concern, currently, the phase control in most TMDs relies on post-growth strategies. Although the scalable and controlled synthesis of 1T'-$MoS(Se)_2$ has been reported recently [72], the development of direct phase-controlled synthesis methods for other materials needs continuous efforts. Very differently, for 2D noble metals, their unusual crystal phases have only been realized via the direct growth under specific synthesis conditions. In other words, transformation from their thermodynamic stable structures to metastable ones has not been achieved via post-growth methods. Nevertheless, reversible crystallinity transition of spherical Pd nanoparticles has been observed previously via the ligand exchange between trioctylphosphine and oleylamine on Pd nanoparticles [151]. It suggests the possibility of achieving the reversible phase transition in 2D noble metals, which requires further investigations.

Furthermore, although polymorphism has been observed in other nanostructures, such as semiconducting III–V compounds (e.g., InAs, GaAs) and II–VI compounds (e.g., ZnS, CdSe) [160,161], few reports have focused on the 2D form of these materials as well as their phase controlled syntheses, which are required to be explored in future.

Lastly, it is interesting that unusual phased noble metals can be used as substrates to guide the epitaxial growth of other metals to achieve unusual crystal structures that cannot be achieved by other methods [162–165]. Such strategy may be extended to TMDs and other layered materials. More importantly, epitaxial growth between different low-dimensional material systems may provide opportunities to further enrich the library of crystal phases.

Acknowledgements This work was supported by the Joint Research Fund for Overseas Chinese, Hong Kong and Macao Scholars (51528201), the MOE under AcRF Tier 2 (ARC 19/15, MOE2014-T2-2-093, MOE2015-T2-2-057, MOE2016-T2-2-103, MOE2017-T2-1-162), AcRF Tier 1 (2016-T1-001-147, 2016-T1-002-051, 2017-T1-001-150, 2017-T1-002-119), and NTU under Start-Up Grant (M4081296.070.500000) in Singapore. We would like to acknowledge the Facility for Analysis, Characterization, Testing and Simulation, Nanyang Technological University, Singapore, for use of their electron microscopy (and/or X-ray) facilities.

Conflict of interest The authors declare that they have no conflict of interest.

1 Novoselov KS, Fal'ko VI, Colombo L, Gellert PR, Schwab MG, Kim K. *Nature*, 2012, 490: 192–200
2 Novoselov KS, Geim AK, Morozov SV, Jiang D, Zhang Y, Dubonos SV, Grigorieva IV, Firsov AA. *Science*, 2004, 306: 666–669
3 Schwierz F. *Nat Nanotech*, 2010, 5: 487–496
4 Chhowalla M, Shin HS, Eda G, Li LJ, Loh KP, Zhang H. *Nat Chem*, 2013, 5: 263–275
5 Manzeli S, Ovchinnikov D, Pasquier D, Yazyev OV, Kis A. *Nat Rev Mater*, 2017, 2: 17033
6 Tan C, Zhang H. *Chem Soc Rev*, 2015, 44: 2713–2731
7 Wang QH, Kalantar-Zadeh K, Kis A, Coleman JN, Strano MS. *Nat Nanotech*, 2012, 7: 699–712
8 Zhang X, Lai Z, Ma Q, Zhang H. *Chem Soc Rev*, 2018, 47: 3301–3338
9 Fiori G, Bonaccorso F, Iannaccone G, Palacios T, Neumaier D, Seabaugh A, Banerjee SK, Colombo L. *Nat Nanotech*, 2014, 9: 768–779
10 Tan C, Cao X, Wu XJ, He Q, Yang J, Zhang X, Chen J, Zhao W, Han S, Nam GH, Sindoro M, Zhang H. *Chem Rev*, 2017, 117: 6225–6331
11 Xu M, Liang T, Shi M, Chen H. *Chem Rev*, 2013, 113: 3766–3798
12 Seo J, Jang J, Park S, Kim C, Park B, Cheon J. *Adv Mater*, 2008, 20: 4269–4273
13 Li L, Chen Z, Hu Y, Wang X, Zhang T, Chen W, Wang Q. *J Am Chem Soc*, 2013, 135: 1213–1216

14 Zhao LD, Lo SH, Zhang Y, Sun H, Tan G, Uher C, Wolverton C, Dravid VP, Kanatzidis MG. *Nature*, 2014, 508: 373–377
15 Xia J, Zhu D, Wang L, Huang B, Huang X, Meng XM. *Adv Funct Mater*, 2015, 25: 4255–4261
16 Wang X, Li Y, Huang L, Jiang XW, Jiang L, Dong H, Wei Z, Li J, Hu W. *J Am Chem Soc*, 2017, 139: 14976–14982
17 Huang X, Tang S, Mu X, Dai Y, Chen G, Zhou Z, Ruan F, Yang Z, Zheng N. *Nat Nanotech*, 2010, 6: 28–32
18 Cheng L, Wang C, Feng L, Yang K, Liu Z. *Chem Rev*, 2014, 114: 10869–10939
19 Duan H, Yan N, Yu R, Chang CR, Zhou G, Hu HS, Rong H, Niu Z, Mao J, Asakura H, Tanaka T, Dyson PJ, Li J, Li Y. *Nat Commun*, 2014, 5: 3093
20 Chen A, Ostrom C. *Chem Rev*, 2015, 115: 11999–12044
21 Fan Z, Zhang H. *Chem Soc Rev*, 2016, 45: 63–82
22 Zhou X, Zhang Q, Gan L, Li H, Xiong J, Zhai T. *Adv Sci*, 2016, 3: 1600177
23 Trigunayat G. *Solid State Ion*, 1991, 48: 3–70
24 Wilson JA, di Salvo FJ, Mahajan S. *Phys Rev Lett*, 1974, 32: 882–885
25 Wilson JA, Di Salvo FJ, Mahajan S. *Adv Phys*, 1975, 24: 117–201
26 Huang Y, Sutter E, Sadowski JT, Cotlet M, Monti OLA, Racke DA, Neupane MR, Wickramaratne D, Lake RK, Parkinson BA, Sutter P. *ACS Nano*, 2014, 8: 10743–10755
27 Ahn JH, Lee MJ, Heo H, Sung JH, Kim K, Hwang H, Jo MH. *Nano Lett*, 2015, 15: 3703–3708
28 Huang X, Li S, Huang Y, Wu S, Zhou X, Li S, Gan CL, Boey F, Mirkin CA, Zhang H. *Nat Commun*, 2011, 2: 292–297
29 Fan Z, Bosman M, Huang X, Huang D, Yu Y, Ong KP, Akimov YA, Wu L, Li B, Wu J, Huang Y, Liu Q, Eng Png C, Lip Gan C, Yang P, Zhang H. *Nat Commun*, 2015, 6: 7684–7691
30 Cao Y, Fatemi V, Fang S, Watanabe K, Taniguchi T, Kaxiras E, Jarillo-Herrero P. *Nature*, 2018, 556: 43–50
31 McDonnell S, Addou R, Buie C, Wallace RM, Hinkle CL. *ACS Nano*, 2014, 8: 2880–2888
32 Zhu J, Wang Z, Yu H, Li N, Zhang J, Meng JL, Liao M, Zhao J, Lu X, Du L, Yang R, Shi D, Jiang Y, Zhang G. *J Am Chem Soc*, 2017, 139: 10216–10219
33 Voiry D, Goswami A, Kappera R, e Silva CCC, Kaplan D, Fujita T, Chen M, Asefa T, Chhowalla M. *Nat Chem*, 2014, 7: 45–49
34 Benson EE, Zhang H, Schuman SA, Nanayakkara SU, Bronstein ND, Ferrere S, Blackburn JL, Miller EM. *J Am Chem Soc*, 2018, 140: 441–450
35 Li Y, Duerloo KAN, Wauson K, Reed EJ. *Nat Commun*, 2016, 7: 10671
36 Wang Y, Xiao J, Zhu H, Li Y, Alsaid Y, Fong KY, Zhou Y, Wang S, Shi W, Wang Y, Zettl A, Reed EJ, Zhang X. *Nature*, 2017, 550: 487–491
37 Eda G, Yamaguchi H, Voiry D, Fujita T, Chen M, Chhowalla M. *Nano Lett*, 2011, 11: 5111–5116
38 Fan X, Xu P, Zhou D, Sun Y, Li YC, Nguyen MAT, Terrones M, Mallouk TE. *Nano Lett*, 2015, 15: 5956–5960
39 Sun Y, Yang W, Ren Y, Wang L, Lei C. *Small*, 2011, 7: 606–611
40 Nayak AP, Bhattacharyya S, Zhu J, Liu J, Wu X, Pandey T, Jin C, Singh AK, Akinwande D, Lin JF. *Nat Commun*, 2014, 5: 3731–3739
41 Zeng Z, Sun T, Zhu J, Huang X, Yin Z, Lu G, Fan Z, Yan Q, Hng HH, Zhang H. *Angew Chem Int Ed*, 2012, 51: 9052–9056
42 Liu Q, Li X, Xiao Z, Zhou Y, Chen H, Khalil A, Xiang T, Xu J, Chu W, Wu X, Yang J, Wang C, Xiong Y, Jin C, Ajayan PM, Song L. *Adv Mater*, 2015, 27: 4837–4844
43 Kochat V, Apte A, Hachtel JA, Kumazoe H, Krishnamoorthy A, Susarla S, Idrobo JC, Shimojo F, Vashishta P, Kalia R, Nakano A, Tiwary CS, Ajayan PM. *Adv Mater*, 2017, 29: 1703754–1703761
44 Rhodes D, Chenet DA, Janicek BE, Nyby C, Lin Y, Jin W, Edelberg D, Mannebach E, Finney N, Antony A, Schiros T, Klarr T, Mazzoni A, Chin M, Chiu Y, Zheng W, Zhang QR, Ernst F, Dadap JI, Tong X, Ma J, Lou R, Wang S, Qian T, Ding H, Osgood Jr. RM, Paley DW, Lindenberg AM, Huang PY, Pasupathy AN, Dubey M, Hone J, Balicas L. *Nano Lett*, 2017, 17: 1616–1622
45 Kang Y, Najmaei S, Liu Z, Bao Y, Wang Y, Zhu X, Halas NJ, Nordlander P, Ajayan PM, Lou J, Fang Z. *Adv Mater*, 2014, 26: 6467–6471
46 Fan Z, Huang X, Han Y, Bosman M, Wang Q, Zhu Y, Liu Q, Li B, Zeng Z, Wu J, Shi W, Li S, Gan CL, Zhang H. *Nat Commun*, 2015, 6: 6571
47 Splendiani A, Sun L, Zhang Y, Li T, Kim J, Chim CY, Galli G, Wang F. *Nano Lett*, 2010, 10: 1271–1275
48 Cao T, Wang G, Han W, Ye H, Zhu C, Shi J, Niu Q, Tan P, Wang E, Liu B, Feng J. *Nat Commun*, 2012, 3: 887
49 Mak KF, He K, Shan J, Heinz TF. *Nat Nanotech*, 2012, 7: 494–498
50 Zeng H, Dai J, Yao W, Xiao D, Cui X. *Nat Nanotech*, 2012, 7: 490–493
51 Lukowski MA, Daniel AS, Meng F, Forticaux A, Li L, Jin S. *J Am Chem Soc*, 2013, 135: 10274–10277
52 Voiry D, Yamaguchi H, Li J, Silva R, Alves DCB, Fujita T, Chen M, Asefa T, Shenoy VB, Eda G, Chhowalla M. *Nat Mater*, 2013, 12: 850–855
53 Wang H, Lu Z, Xu S, Kong D, Cha JJ, Zheng G, Hsu PC, Yan K, Bradshaw D, Prinz FB, Cui Y. *Proc Natl Acad Sci USA*, 2013, 110: 19701–19706
54 Bertolazzi S, Brivio J, Kis A. *ACS Nano*, 2011, 5: 9703–9709
55 Castellanos-Gomez A, Poot M, Steele GA, van der Zant HSJ, Agraït N, Rubio-Bollinger G. *Adv Mater*, 2012, 24: 772–775
56 Velusamy DB, Kim RH, Cha S, Huh J, Khazaeinezhad R, Kassani SH, Song G, Cho SM, Cho SH, Hwang I, Lee J, Oh K, Choi H, Park C. *Nat Commun*, 2015, 6: 8063–8073
57 Huang X, Zeng Z, Zhang H. *Chem Soc Rev*, 2013, 42: 1934–1946
58 Wilson JA, Yoffe AD. *Adv Phys*, 1969, 18: 193–335
59 Fei Z, Palomaki T, Wu S, Zhao W, Cai X, Sun B, Nguyen P, Finney J, Xu X, Cobden DH. *Nat Phys*, 2017, 13: 677–682
60 Ma X, Guo P, Yi C, Yu Q, Zhang A, Ji J, Tian Y, Jin F, Wang Y, Liu K, Xia T, Shi Y, Zhang Q. *Phys Rev B*, 2016, 94: 214105–214112
61 Duerloo KAN, Li Y, Reed EJ. *Nat Commun*, 2014, 5: 4214–4222
62 Keum DH, Cho S, Kim JH, Choe DH, Sung HJ, Kan M, Kang H, Hwang JY, Kim SW, Yang H, Chang KJ, Lee YH. *Nat Phys*, 2015, 11: 482–486
63 Radisavljevic B, Radenovic A, Brivio J, Giacometti V, Kis A. *Nat Nanotech*, 2011, 6: 147–150
64 Baugher BWH, Churchill HOH, Yang Y, Jarillo-Herrero P. *Nano Lett*, 2013, 13: 4212–4216
65 Kibsgaard J, Chen Z, Reinecke BN, Jaramillo TF. *Nat Mater*, 2012, 11: 963–969
66 Cho S, Kim S, Kim JH, Zhao J, Seok J, Keum DH, Baik J, Choe DH, Chang KJ, Suenaga K, Kim SW, Lee YH, Yang H. *Science*, 2015, 349: 625–628
67 Kappera R, Voiry D, Yalcin SE, Branch B, Gupta G, Mohite AD, Chhowalla M. *Nat Mater*, 2014, 13: 1128–1134
68 Yoshida M, Ye J, Zhang Y, Imai Y, Kimura S, Fujiwara A, Nishizaki T, Kobayashi N, Nakano M, Iwasa Y. *Nano Lett*, 2017, 17: 5567–5571
69 Zeng Z, Yin Z, Huang X, Li H, He Q, Lu G, Boey F, Zhang H. *Angew Chem Int Ed*, 2011, 50: 11093–11097
70 Yang K, Wang X, Li H, Chen B, Zhang X, Li S, Wang N, Zhang H, Huang X, Huang W. *Nanoscale*, 2017, 9: 5102–5109
71 Li H, Chen S, Jia X, Xu B, Lin H, Yang H, Song L, Wang X. *Nat Commun*, 2017, 8: 15377–15387
72 Yu Y, Nam GH, He Q, Wu XJ, Zhang K, Yang Z, Chen J, Ma Q, Zhao M, Liu Z, Ran FR, Wang X, Li H, Huang X, Li B, Xiong Q, Zhang Q, Liu Z, Gu L, Du Y, Huang W, Zhang H. *Nat Chem*, 2018, 10: 638–643
73 Yu P, Lin J, Sun L, Le QL, Yu X, Gao G, Hsu CH, Wu D, Chang TR, Zeng Q, Liu F, Wang QJ, Jeng HT, Lin H, Trampert A, Shen Z, Suenaga K, Liu Z. *Adv Mater*, 2017, 29: 1603991–1603998
74 Lin YC, Dumcenco DO, Huang YS, Suenaga K. *Nat Nanotech*, 2014,

9: 391–396
75 Zhou L, Zubair A, Wang Z, Zhang X, Ouyang F, Xu K, Fang W, Ueno K, Li J, Palacios T, Kong J, Dresselhaus MS. *Adv Mater*, 2016, 28: 9526–9531
76 Song S, Keum DH, Cho S, Perello D, Kim Y, Lee YH. *Nano Lett*, 2016, 16: 188–193
77 Zhou L, Xu K, Zubair A, Liao AD, Fang W, Ouyang F, Lee YH, Ueno K, Saito R, Palacios T, Kong J, Dresselhaus MS. *J Am Chem Soc*, 2015, 137: 11892–11895
78 Guo Y, Sun D, Ouyang B, Raja A, Song J, Heinz TF, Brus LE. *Nano Lett*, 2015, 15: 5081–5088
79 Dines MB. *J Chem Educ*, 1974, 51: 221–223
80 Dines MB. *Mater Res Bull*, 1975, 10: 287–291
81 Somoano RB, Hadek V, Rembaum A. *J Chem Phys*, 1973, 58: 697–701
82 Whittingham MS. *Chem Rev*, 2004, 104: 4271–4302
83 Eda G, Fujita T, Yamaguchi H, Voiry D, Chen M, Chhowalla M. *ACS Nano*, 2012, 6: 7311–7317
84 Chrissafis K, Zamani M, Kambas K, Stoemenos J, Economou NA, Samaras I, Julien C. *Mater Sci Eng-B*, 1989, 3: 145–151
85 Jiménez Sandoval S, Yang D, Frindt RF, Irwin JC. *Phys Rev B*, 1991, 44: 3955–3962
86 Yang D, Sandoval SJ, Divigalpitiya WMR, Irwin JC, Frindt RF. *Phys Rev B*, 1991, 43: 12053–12056
87 Young VG, McKelvy MJ, Glaunsinger WS, Von Dreele RB. *Chem Mater*, 1990, 2: 75–81
88 Enyashin AN, Yadgarov L, Houben L, Popov I, Weidenbach M, Tenne R, Bar-Sadan M, Seifert G. *J Phys Chem C*, 2011, 115: 24586–24591
89 Rocquefelte X, Boucher F, Gressier P, Ouvrard G, Blaha P, Schwarz K. *Phys Rev B*, 2000, 62: 2397–2400
90 Kan M, Wang JY, Li XW, Zhang SH, Li YW, Kawazoe Y, Sun Q, Jena P. *J Phys Chem C*, 2014, 118: 1515–1522
91 Gao G, Jiao Y, Ma F, Jiao Y, Waclawik E, Du A. *J Phys Chem C*, 2015, 119: 13124–13128
92 Heising J, Kanatzidis MG. *J Am Chem Soc*, 1999, 121: 638–643
93 Cheng Y, Nie A, Zhang Q, Gan LY, Shahbazian-Yassar R, Schwingenschlogl U. *ACS Nano*, 2014, 8: 11447–11453
94 Wang L, Xu Z, Wang W, Bai X. *J Am Chem Soc*, 2014, 136: 6693–6697
95 Luo H, Xie W, Tao J, Inoue H, Gyenis A, Krizan JW, Yazdani A, Zhu Y, Cava RJ. *Proc Natl Acad Sci USA*, 2015, 112: E1174–E1180
96 Npwnpnny RJJ. *Am Mineral*, 1974, 64: 758–767
97 Johari P, Shenoy VB. *ACS Nano*, 2012, 6: 5449–5456
98 Mitchell RS, Fujiki Y, Ishizawa Y. *Nature*, 1974, 247: 537–538
99 Pałosz B, Steurer W, Schulz H. *Acta Crystlogr B Struct Sci*, 1990, 46: 449–455
100 Zhou X, Zhang Q, Gan L, Li H, Zhai T. *Adv Funct Mater*, 2016, 26: 4405–4413
101 Bilousov OV, Ren Y, Törndahl T, Donzel-Gargand O, Ericson T, Platzer-Björkman C, Edoff M, Hägglund C. *Chem Mater*, 2017, 29: 2969–2978
102 Zhou X, Gan L, Tian W, Zhang Q, Jin S, Li H, Bando Y, Golberg D, Zhai T. *Adv Mater*, 2015, 27: 8035–8041
103 Ramakrishna Reddy KT, Koteswara Reddy N, Miles RW. *Sol Energy Mater Sol Cells*, 2006, 90: 3041–3046
104 Sinsermsuksakul P, Sun L, Lee SW, Park HH, Kim SB, Yang C, Gordon RG. *Adv Energy Mater*, 2014, 4: 1400496
105 Xia J, Li XZ, Huang X, Mao N, Zhu DD, Wang L, Xu H, Meng XM. *Nanoscale*, 2016, 8: 2063–2070
106 Tian Z, Guo C, Zhao M, Li R, Xue J. *ACS Nano*, 2017, 11: 2219–2226
107 Patel M, Chavda A, Mukhopadhyay I, Kim J, Ray A. *Nanoscale*, 2016, 8: 2293–2303
108 Su G, Hadjiev VG, Loya PE, Zhang J, Lei S, Maharjan S, Dong P, M.~Ajayan P, Lou J, Peng H. *Nano Lett*, 2015, 15: 506–513
109 Hu Y, Luo B, Ye D, Zhu X, Lyu M, Wang L. *Adv Mater*, 2017, 29: 1606132
110 Qu B, Ma C, Ji G, Xu C, Xu J, Meng YS, Wang T, Lee JY. *Adv Mater*, 2014, 26: 3854–3859
111 Ye G, Gong Y, Lei S, He Y, Li B, Zhang X, Jin Z, Dong L, Lou J, Vajtai R, Zhou W, Ajayan PM. *Nano Res*, 2017, 10: 2386–2394
112 Brent JR, Lewis DJ, Lorenz T, Lewis EA, Savjani N, Haigh SJ, Seifert G, Derby B, O'Brien P. *J Am Chem Soc*, 2015, 137: 12689–12696
113 Fernandes PA, Sousa MG, Salomé PMP, Leitão JP, da Cunha AF. *CrystEngComm*, 2013, 15: 10278–10286
114 Huang Y, Xu K, Wang Z, Shifa TA, Wang Q, Wang F, Jiang C, He J. *Nanoscale*, 2015, 7: 17375–17380
115 Zhou T, Pang WK, Zhang C, Yang J, Chen Z, Liu HK, Guo Z. *ACS Nano*, 2014, 8: 8323–8333
116 Sutter E, Huang Y, Komsa HP, Ghorbani-Asl M, Krasheninnikov AV, Sutter P. *Nano Lett*, 2016, 16: 4410–4416
117 Mitchell RS, Fujiki Y, Ishizawa Y. *J Cryst Growth*, 1982, 57: 273–279
118 Schnering HG, Wiedemeier H. *Z Kristallogr-Crystline Mater*, 1981, 156: 143–150
119 Chattopadhyay T, Pannetier J, Von Schnering HG. *J Phys Chem Solids*, 1986, 47: 879–885
120 Bletskan DI. *J Ovonic Res*, 2005, 61–69
121 Tian Z, Zhao M, Xue X, Xia W, Guo C, Guo Y, Feng Y, Xue J. *ACS Appl Mater Interfaces*, 2018, 10: 12831–12838
122 Sharma RC, Chang YA. *Bull Alloy Phase Diagrams*, 1986, 7: 68–72
123 Jain PK, Huang X, El-Sayed IH, El-Sayed MA. *Acc Chem Res*, 2008, 41: 1578–1586
124 Qin HL, Wang D, Huang ZL, Wu DM, Zeng ZC, Ren B, Xu K, Jin J. *J Am Chem Soc*, 2013, 135: 12544–12547
125 Saleem F, Zhang Z, Xu B, Xu X, He P, Wang X. *J Am Chem Soc*, 2013, 135: 18304–18307
126 Fan Z, Huang X, Tan C, Zhang H. *Chem Sci*, 2015, 6: 95–111
127 Li Q, Wu L, Wu G, Su D, Lv H, Zhang S, Zhu W, Casimir A, Zhu H, Mendoza-Garcia A, Sun S. *Nano Lett*, 2015, 15: 2468–2473
128 Liu X, Luo J, Zhu J. *Nano Lett*, 2006, 6: 408–412
129 Eustis S, el-Sayed MA. *Chem Soc Rev*, 2006, 35: 209–217
130 Xia Y, Xiong Y, Lim B, Skrabalak SE. *Angew Chem Int Ed*, 2009, 48: 60–103
131 Huang B, Kobayashi H, Yamamoto T, Matsumura S, Nishida Y, Sato K, Nagaoka K, Kawaguchi S, Kubota Y, Kitagawa H. *J Am Chem Soc*, 2017, 139: 4643–4646
132 Zhang Q, Kusada K, Wu D, Yamamoto T, Toriyama T, Matsumura S, Kawaguchi S, Kubota Y, Kitagawa H. *Nat Commun*, 2018, 9: 510
133 Chakraborty I, Shirodkar SN, Gohil S, Waghmare UV, Ayyub P. *J Phys-Condens Matter*, 2014, 26: 025402
134 Kusada K, Kobayashi H, Yamamoto T, Matsumura S, Sumi N, Sato K, Nagaoka K, Kubota Y, Kitagawa H. *J Am Chem Soc*, 2013, 135: 5493–5496
135 Huang X, Li H, Li S, Wu S, Boey F, Ma J, Zhang H. *Angew Chem Int Ed*, 2011, 50: 12245–12248
136 Liao H, Zhu J, Hou Y. *Nanoscale*, 2014, 6: 1049–1055
137 Fan Z, Zhu Y, Huang X, Han Y, Wang Q, Liu Q, Huang Y, Gan CL, Zhang H. *Angew Chem Int Ed*, 2015, 54: 5672–5676
138 Fan Z, Chen Y, Zhu Y, Wang J, Li B, Zong Y, Han Y, Zhang H. *Chem Sci*, 2017, 8: 795–799
139 Guo Q, Zhao Y, Mao WL, Wang Z, Xiong Y, Xia Y. *Nano Lett*, 2008, 8: 972–975
140 Diao J, Gall K, Dunn ML. *Nat Mater*, 2003, 2: 656–660
141 Kondo Y, Takayanagi K. *Science*, 2000, 289: 606–608
142 Chakraborty I, Carvalho D, Shirodkar SN, Lahiri S, Bhattacharyya S, Banerjee R, Waghmare U, Ayyub P. *J Phys-Condens Matter*, 2011, 23: 325401–325412
143 Gao K, Wang Y, Wang Z, Zhu Z, Wang J, Luo Z, Zhang C, Huang X, Zhang H, Huang W. *Chem Commun*, 2018, 54: 4613–4616
144 Kitchin JR, Nørskov JK, Barteau MA, Chen JG. *Phys Rev Lett*, 2004, 93: 156801

145 Titmuss S, Wander A, King DA. *Chem Rev*, 1996, 96: 1291–1306
146 Vericat C, Vela ME, Benitez G, Carro P, Salvarezza RC. *Chem Soc Rev*, 2010, 39: 1805–1834
147 Ghosh Chaudhuri R, Paria S. *Chem Rev*, 2012, 112: 2373–2433
148 Jiang HL, Akita T, Ishida T, Haruta M, Xu Q. *J Am Chem Soc*, 2011, 133: 1304–1306
149 Wang D, Xin HL, Hovden R, Wang H, Yu Y, Muller DA, DiSalvo FJ, Abruña HD. *Nat Mater*, 2012, 12: 81–87
150 Kim YH, Jun Y, Jun BH, Lee SM, Cheon J. *J Am Chem Soc*, 2002, 124: 13656–13657
151 Liu Y, Wang C, Wei Y, Zhu L, Li D, Jiang JS, Markovic NM, Stamenkovic VR, Sun S. *Nano Lett*, 2011, 11: 1614–1617
152 Huang X, Li S, Wu S, Huang Y, Boey F, Gan CL, Zhang H. *Adv Mater*, 2012, 24: 979–983
153 Rajaji V, Dutta U, Sreeparvathy PC, Sarma SC, Sorb YA, Joseph B, Sahoo S, Peter SC, Kanchana V, Narayana C. *Phys Rev B*, 2018, 97: 085107
154 Besson JM, Itié JP, Polian A, Weill G, Mansot JL, Gonzalez J. *Phys Rev B*, 1991, 44: 4214–4234
155 Qi Y, Shi W, Naumov PG, Kumar N, Sankar R, Schnelle W, Shekhar C, Chou FC, Felser C, Yan B, Medvedev SA. *Adv Mater*, 2017, 29: 1605965
156 Tran MK, Levallois J, Lerch P, Teyssier J, Kuzmenko AB, Autès G, Yazyev OV, Ubaldini A, Giannini E, van der Marel D, Akrap A. *Phys Rev Lett*, 2014, 112: 047402
157 Mao HK, Bell PM, Shaner JW, Steinberg DJ. *J Appl Phys*, 1978, 49: 3276–3283
158 McMahon MI, Nelmes RJ. *Chem Soc Rev*, 2006, 35: 943–963
159 Koski KJ, Kamp NM, Smith RK, Kunz M, Knight JK, Alivisatos AP. *Phys Rev B*, 2008, 78: 165410
160 Tong CJ, Zhang H, Zhang YN, Liu H, Liu LM. *J Mater Chem A*, 2014, 2: 17971–17978
161 Singh AK, Zhuang HL, Hennig RG. *Phys Rev B*, 2014, 89: 245431
162 Fan Z, Zhang H. *Acc Chem Res*, 2016, 49: 2841–2850
163 Fan Z, Huang X, Chen Y, Huang W, Zhang H. *Nat Protoc*, 2017, 12: 2367–2378
164 Lu Q, Wang AL, Gong Y, Hao W, Cheng H, Chen J, Li B, Yang N, Niu W, Wang J, Yu Y, Zhang X, Chen Y, Fan Z, Wu XJ, Chen J, Luo J, Li S, Gu L, Zhang H. *Nat Chem*, 2018, 10: 456–461
165 Tan C, Chen J, Wu XJ, Zhang H. *Nat Rev Mater*, 2018, 3: 17089